

Three-dimensional conductive heat transfer topology optimisation in a cubic domain for the volume-to-surface problem

Francois H. Burger, Jaco Dirker*, Josua P. Meyer**

*Department of Mechanical and Aeronautical Engineering, University of Pretoria, Pretoria, Private Bag X20,
Hatfield 0028, South Africa.*

**Corresponding Author:*

Email Address: jaco.dirker@up.ac.za

Phone: +27 (0)12 420 2465

***Alternative Corresponding Author:*

Email Address: josua.meyer@up.ac.za

Phone +27 (0)12 420 3104

ABSTRACT

In this paper, three-dimensional topology optimisation was investigated with regard to heat conduction for the volume-to-point or volume-to-surface problem in a cubic three-dimensional domain. The positioning of high conductive material in a solid with low thermal conductivity and high heat generation was optimized via the method of moving asymptotes (MMA) algorithm in order to reduce the average internal temperature. Both partial and full Dirichlet temperature boundaries were considered. Thermal conductivity ratios ranging from 5 to 3 000 and volumetric constraint between 5% and 30% were covered. The high conductive material distributions were found to resemble those of natural tree-structures, with the four primary branches extending towards the furthest corners of the domain when a single seed-location was used. Multiple seed locations (two and four) were also considered. It was found that each seed location resulted in a separate conduction tree, each of which also had four primary branches. By increasing the number of seed locations from one to four, the thermal performance of the optimized internal architecture improved by up to 20% for a volumetric constraint of 5%.

Keywords: topology optimisation, conduction, three-dimensional

Nomenclature

a	finite volume method matrix coefficient
$[A]$	matrix of linear equation
\mathbf{b}	source term vector
c	characteristic length of temperature boundary/seed location
D	diagonal section plane
g_0	objective function
g_1	constraint function
H_b	height of fixed subdomain
H_D	dimension of domain in the z -direction
I	number of optimisation iterations
k_L	low thermal conductivity in the heat-generating solid
k_H	high thermal conductivity
k	cell thermal conductivity
k^*	thermal conductivity ratio
L	lower asymptote
L_D	dimension of domain in the y -direction
M	number of nodes for x -, y - or z -direction
M_Ω	total number of nodes in the domain
n	normal direction
O	origin/reference point

p	intermediate density penalisation factor
q	cell heat generation density
q_H	high heat generation density
s	optimisation algorithm moving asymptote parameter
s_0	optimisation algorithm fixed asymptote parameter
T	temperature
\bar{T}	average temperature
\mathbf{T}	temperature vector
U	upper asymptote
v	cell/element volume
V_f	volume ratio occupied by high conductive material
V^*	maximum allowed volume ratio occupied by high conductive material
W_D	dimension of domain in the x -direction
x	x -direction / x -coordinate
y	y -direction / y -coordinate
z	z -direction

Greek Symbols

λ	adjoint vector
θ	design variable/cellular density
$\boldsymbol{\theta}$	design variable vector/density vector

κ MMA algorithm iteration number

τ dimensionless temperature measure

Subscripts

1 Referring to the single-seed case

2 Referring to the two-seed case

4 Referring to the four-seed case

i index number

j index number

max maximum

∞ temperature boundary

Superscripts

T transpose

1. Introduction

One of the major limiting factors in the increase of power density in electronics is the thermal barrier opposing the transport of internally generated heat to cooler regions. The scale of electronics is becoming smaller, which thus increases the need for small-scale cooling solutions. At smaller dimensional scales, conventional electronic cooling, whether it is single-phase convection, or evaporative and boiling convection, is challenging, since there is limited space for fluid channels and the support systems needed to maintain the operation of these systems. This makes internal conduction cooling, where heat is distributed to the surface regions, a viable solution on a small scale, on condition that only a limited volume percentage is set aside for this purpose.

This limited space problem has sparked numerous papers in recent years where the goal generally is the minimisation of the thermal resistance in a volume using high conductive cooling paths. The volume-to-point, or volume-to-surface problem thus requires finding the best internal distribution of a finite quantity of high conductive material which could aid in the heat transport from within a uniformly heated volume to predefined regions on its boundary. The result of such optimisation drives is measured as a reduction in overall temperatures within such a volume.

Some of the first works in the heat conduction volume-to-point problem were done by Bejan and co-workers [1-7] for rectangular and other geometrically shaped bodies using the constructal theory approach. Among their numerous works in this area, Bejan *et al.* [8] also considered two-dimensional conduction optimisation at micro- and nano-scales where traditional conduction heat transfer theory is not suitable. One of the methods that were followed was the deterministic approach where predefined geometric shape-types (such as linear rectangular paths perpendicular branching paths) were considered. This deterministic geometrical choice has a significant advantage from a manufacturing point of view. Previous work by the current authors also considered preselected geometrical types such as conductive embedded plate structures in power electronic modules in order to increase the effective power density [9-11].

Such preselected geometrical types, however, impose restrictions and may be far from the overall optimum material distribution as shown by Boichot *et al.* [12] and Song and Guo [13]. In recent years, topology optimisation tools have been used to solve the volume-to-point problem with heat conduction in both the discrete and continuous design methods. The internal material distribution is represented in a structured manner

by a set of design variables. Gersborg-Hansen *et al.* [14], Zhang and Liu [15] and Dirker and Meyer [16] investigated the two-dimensional optimisation of conducting paths using the solid isotropic with material penalisation (SIMP) method coupled to a multi-dimensional optimisation algorithm. It was found that the optimal paths obtained by this method, were similar to those of natural trees.

Other topology optimisation schemes also exist. Li *et al.* [17-18] investigated two-dimensional heat conduction using evolutionary structural optimisation. Gao *et al.* [19] investigated two-dimensional conduction problems using a modified bi-directional evolutionary structural optimisation scheme, which is very similar to Evolutionary Structural Optimisation. Boichot *et al.* [12] investigated cellular automaton with the goal of effectively cooling a heat-generating surface by arranging the configuration of high conductive material links. Cheng *et al.* [20] and Song and Guo [13] implemented bionic optimisation in the construction of highly effective heat conduction paths. Xu *et al.* [21] investigated the volume-to-point (VP) problem using simulated annealing, which proved to perform better than constructal theory and bionic optimisation. All of these studies obtained internal material distributions that resembled natural-looking tree structures.

Mostly two-dimensional optimisation studies have been conducted and limited three-dimensional optimisation results are available. Bejan and co-workers [22-23] and Feng *et al.* [24] did consider three-dimensional cases, but mostly cylindrical and conical type domains were considered using constructal theory. For the rectangular and cubic domains, few results are available and is difficult to generalise. Since almost all two-dimensional topology optimisation studies have exhibited non-perpendicular heat flow in the two dimensions considered, it is logical that this will also be the case in the third dimension, and that the third dimension must be included in the optimisation process to better understand the type of optimized geometry in real-world three-dimensional cases. Also, because a two-dimensional approach is not able to describe the impact of the size of a Dirichlet boundary type in the third dimension, a three-dimensional approach has become vital, at least in this investigation.

The SIMP approach, even though it does not supply discrete material distributions, allows for additional flexibility in the material density and has been accepted widely among both engineers and researchers interested in topology optimization in a variety of fields [25]. For thermal conduction topology optimization in specific, [14,15] showed that SIMP is a plausible approach. The MMA algorithm and its family of algorithms are widely accepted for topology optimization problems which are restricted by either a single constraint or multiple

constraints. This algorithm has attracted significant interest from the topology optimization community [26, 27] and is for this reason adopted for this investigation.

The purpose of this study is thus to consider three-dimensional optimisation for the volume-to-surface problem where the average domain temperature is to be minimized. Topology optimisation and specifically the method of moving asymptotes [28] algorithm, together with the SIMP method are used to determine the optimised internal architectures in a cubic three-dimensional domain for different thermal conductivity combinations, volume constraint, boundary types and boundary placement options. Due to the computational expense of performing sensitivity analyses needed during the MMA approach, (especially since a large number of design variables are needed), the adjoint method is used.

2. Problem Formulation

Consider a cubic domain \emptyset , shown in Figure 1 with $L_D = W_D = H_D$ [m]. The domain originally contains only a solid with a low uniform thermal conductivity of k_L [W/mK] and high uniform volumetric heat-generating rate of q_H [W/m³]. The heat-generating rate is directly linked to the function of the solid (ie. it could be representative of for instance, an electronic module which has an internal volumetric heat generation). All boundaries are adiabatic except for a square region having a characteristic length of c [m] centred on one of the external surfaces. This portion has a constant uniform temperature of T_∞ [K]. High conductive material having a conductivity of k_H is to be introduced by replacing the original low conductive material to aid heat transport towards the constant temperature region on the boundary. In order to numerically determine the optimized material distribution, the domain is divided into M_Ω number of equally sized smaller cubic sub-volumes (or elements), each with a volume of v [m³], which fill the entire domain in a structured manner. The volumetric density of the high thermal conductive material in each element (uniform within the element), is described by a design variable θ_i , which can take any value between 0 and 1. The thermal conductivity within the element is thus given by:

$$k(\theta_i) = k_L + \theta_i(k_H - k_L) \quad (1)$$

Index i refers to the element number. Likewise, the local heat generation rate within an element is given by:

$$q(\theta_i) = q_H(1 - \theta_i) \quad (2)$$

When $\theta_i = 0$, the element has a low thermal conductivity of k_L and a high heat-generating rate of q_H , while when $\theta_i = 1$, the element has the maximum thermal conductivity of k_H and no heat-generation (representing a volumetric region occupied fully by the high thermal conductive material).

The purpose of the optimisation process is to find the optimal material distribution (described by the density vector $\boldsymbol{\theta}$) that would minimise an objective function, $g_0(\mathbf{T})$ (where \mathbf{T} is the temperature vector containing the temperatures of all elements in the domain, which is a function of $\boldsymbol{\theta}$), subject to a non-uniform heat generation field (described by the design variable dependence given in Eq. (2)) while adhering to one (or more) constraint(s), $g_1(\boldsymbol{\theta})$. Average temperature, \bar{T} , is selected as the objective function in this paper. Other objective functions can also be used, however, in a previous investigation [16], the average temperature was shown to be suitable. There is only one constraint in this paper, namely that the volume ratio, V_f , which the high conductive material occupies, is smaller than some maximum allowed proportion, V^* .

This is formulated mathematically as:

Find: $\boldsymbol{\theta}$

$$\text{Minimise: } g_0(\mathbf{T}) = \bar{T} = \frac{1}{M_\Omega} \sum_{i=1}^{M_\Omega} T_i \quad (3)$$

$$\text{Subject to: } g_1(\boldsymbol{\theta}) = V_f = \frac{1}{M_\Omega} \sum_{i=1}^{M_\Omega} \theta_i \leq V^* \quad (4)$$

3. Numerical Method

3.1. Finite Volume Method

To solve the temperature distribution in the domain, the finite volume method (FVM) is adopted. Each element is represented by a single volume-centred node. Assuming steady-state diffusion, the energy equation reduces to:

$$\frac{\partial}{\partial x} \left(k(\theta) \frac{\partial T}{\partial x} \right) + \frac{\partial}{\partial y} \left(k(\theta) \frac{\partial T}{\partial y} \right) + \frac{\partial}{\partial z} \left(k(\theta) \frac{\partial T}{\partial z} \right) + q(\theta) = 0 \quad (5)$$

At the external boundaries, the following is applicable:

$$T = T_\infty \text{ at the temperature boundary} \quad (6)$$

$$\frac{dT}{dn} = 0 \text{ except at the temperature boundary} \quad (7)$$

Following the FVM derivation, the following holds for a multidimensional domain for element number i not on a diabatic domain boundary:

$$T_i \sum_{j=1}^{M_\Omega} (a_j) = \sum_{j=1}^{M_\Omega} (a_j T_j) + q(\theta_i) v \quad (8)$$

where $i \neq j$. Coefficients a_j are calculated using the thermal conductivity value at the interface of two neighbouring elements, the nodal distance between the elements and the heat flux area (for all non-neighbouring elements, $a_j = 0$). The thermal conductivity is calculated using the harmonic mean of the conductivity values on either side of the interface, k_j and k_i , assuming the element lengths of both are equal:

$$k = \frac{2k_i k_j}{k_i + k_j} \quad (9)$$

For an element on a diabatic domain boundary, a similar equation to Eq. (8) can be drawn up, which would contain an additional boundary heat term [W] on the right-hand side. Such equations are used to describe each element in the domain and to set up a matrix, $[A]$, of linear equations that is solved using an iterative solver:

$$[A]\mathbf{T} = \mathbf{b} \quad (10)$$

Vector \mathbf{b} contains all source terms (generated heat) as well as boundary heat terms on diabatic boundaries. The accuracy of the numerical model was checked against the results of commercial numerical packages.

3.1. Method of Moving Asymptotes

The method of moving asymptotes algorithm [28] is used to solve a non-linear optimisation problem by introducing a strictly convex sub-problem. It is based on the first-order Taylor series expansion of the objective and the constraint functions. The MMA has been shown to be well suited for structural and, multidisciplinary optimization applications, especially where reciprocal or reciprocal-like approximations are used [27]. In broad terms, the following iterative scheme is used (for more information on this method the reader is referred to the original text):

STEP 0) A starting point $\boldsymbol{\theta}^{(0)}$ is chosen for iteration $\kappa = 0$

STEP I) For a given iteration, κ , the following are determined:

- i. Constraint function value: $g_1(\boldsymbol{\theta}^{(\kappa)})$
- ii. Gradients (in terms of θ) of the cost function as well as the constraint functions: $\nabla g_0(\boldsymbol{\theta}^{(\kappa)})$
and $\nabla g_1(\boldsymbol{\theta}^{(\kappa)})$

STEP II) Generate a sub-problem based on the original problem by replacing the original implicit functions with approximating explicit functions based on the results of STEP I.

STEP III) Find the optimal solution of the sub-problem and let this solution be the next iteration point $\boldsymbol{\theta}^{(\kappa+1)}$.
Go to STEP I) and repeat until some convergence criterion is met.

The MMA algorithm uses moving asymptotes to relax or restrict the optimization process depending on whether it is slow and monotone, or oscillating. These asymptotes are re-calculated for each iteration and are dependent on the current density vector $\boldsymbol{\theta}$ as well as additional information from previous optimisation iterations. During the first two MMA iterations ($\kappa = 0$ and $\kappa = 1$) when historic data is not yet available, all lower asymptotes (for each design variable, indexed i) were set to $L_i^{(\kappa)} = -s_0$, while all upper asymptotes were set to $U_i^{(\kappa)} = s_0$. For MMA iteration number 2 and above, the lower asymptote for each design variable was set to $L_i^{(\kappa)} = \theta_i^{(\kappa)} - s[\theta_i^{(\kappa-1)} - L_i^{(\kappa-1)}]$ when the process started to oscillate, or $L_i^{(\kappa)} = \theta_i^{(\kappa)} - [\theta_i^{(\kappa-1)} - L_i^{(\kappa-1)}]/s$ when the asymptote slowed the process down. Likewise, the upper asymptote for each design variable was either set to $U_i^{(\kappa)} = \theta_i^{(\kappa)} + s[U_i^{(\kappa-1)} - \theta_i^{(\kappa-1)}]$ or $U_i^{(\kappa)} = \theta_i^{(\kappa)} + [U_i^{(\kappa-1)} - \theta_i^{(\kappa-1)}]/s$. The values of s_0 and s were carefully selected in this investigation to produce the lowest optimized value of $g_0(\mathbf{T})$. This is discussed later in the paper.

3.2. Penalisation Method

The MMA algorithm has the freedom to assign any value from 0 to 1 to each θ in order to minimize the objective function (non-discrete). The purpose of the SIMP method is to penalise the intermediate densities (non-integer θ values) and encourage the optimisation algorithm to produce 0-1 solutions, although intermediate densities are still possible.

The temperature distribution required in the MMA algorithm is based on conductivity and heat generation densities calculated using equations (1) and (2). The MMA also requires the sensitivities of the objective

function, which can be calculated on penalised density values, instead of the densities of the actual material distribution. This is where the SIMP method is introduced. Equations (1) and (2) are altered as follows:

$$k(\theta_i) = k_L + \theta_i^p (k_H - k_L) \quad (11)$$

$$q(\theta_i) = q_H (1 - \theta_i^p) \quad (12)$$

Here p is the penalisation factor and can take on a value greater than or equal to 1.

3.3. Adjoint Method

The sensitivity field of the objection function is required by the MMA algorithm. This could be calculated directly, but would be complex and extremely computationally expensive, especially since there are a large number of design variables. The adjoint method provides an efficient option for calculating the sensitivity field of the objective function, $dg_0/d\theta$ and has successfully been implemented in volume-to-point/surface (VP) heat conduction problems in the past [14,16].

Each design variable sensitivity was calculated by using the adjoint equation [29]:

$$\frac{dg_0}{d\theta_i} = \frac{\partial g_0}{\partial \theta_i} - \boldsymbol{\lambda}^T \left(\frac{\partial [A]}{\partial \theta_i} \mathbf{T} - \frac{\partial \mathbf{b}}{\partial \theta_i} \right) \quad (13)$$

This equation is used to calculate the sensitivity of each element according to the objective function, thus it forms a matrix of sensitivities, which is sent to the MMA algorithm. The adjoint vector, $\boldsymbol{\lambda}$, is calculated as follows:

$$[A]^T \boldsymbol{\lambda} = \left(\frac{\partial g_0}{\partial \mathbf{T}} \right)^T \quad (14)$$

where $[A]$ is the conductivity matrix and g_0 is the objective function. The rest of the terms in Eq. (13) are calculated easily. $\partial g_0/\partial \theta_i$ is zero since the calculation of the objective function is not directly dependent on the density of an element. $\partial [A]/\partial \theta_i$ and $\partial \mathbf{b}/\partial \theta_i$ are calculated by only deriving the parts in the matrix or vector that are dependent on θ_i .

3.4. Non-Dimensional Temperature Measure

It was found that the difference between the peak temperature in the domain, T_{max} , and the boundary temperature T_∞ , is directly proportional to, q_H , and L_D^2 and indirectly proportional to the thermal conductivity inside the domain. From this, a non-dimensional temperature measure, τ , can be defined to represent the thermal

performance of a given high conductive material distribution, and which can be used to compare the thermal performance of a particular material distribution to another:

$$\tau = \frac{(T_{max} - T_{\infty})k_L}{q_H L_D^2} \quad (15)$$

Other investigations that also used such a measure include [22, 30]. Low τ values indicate good thermal cooling performance of the material distribution while higher τ values represent poorer thermal performance. It was found that τ is dependent on both k_L and k_H . However, if these are in a fixed ratio to each other, i.e.: $k_H/k_L =$ constant, the thermal dependence on τ is fully described by either k_L or k_H . In addition, the converged material distribution is then independent of the individual thermal conductivities of k_L or k_H , but rather becomes dependent on the thermal conductivity ratio defined as:

$$k^* = k_H/k_L \quad (16)$$

The heavy dependence of τ on V^* (volumetric constraint ratio) will be discussed later.

It might be noted that the objective function in this investigation is the average domain temperature, while the temperature measure, τ , of Eq. (15) uses the peak temperature in the domain. These are not strictly speaking equivalent, however, it has been found that their relative behaviour is very similar for the conditions covered here. In order to conform to previously published results [16], the use of τ is adopted in this paper. Also, it would be exceedingly computationally expensive to redefine the objective function to be equal to the peak domain temperature, since the adjoint method is not suitably convenient for this, and also it has been shown that the use of the peak domain temperature as objective resulted in poorer performing material distributions [16].

3.5. Dependence Investigation

Investigations were made to check the dependence of the optimized layout on the numeric mesh density, the number of MMA iterations, penalisation scheme and initial density distributions. It was found that $M = 50$ elements along the characteristic length (L_D) were sufficient and that element numbers beyond this only resulted in marginal thermal improvements. Similarly, it was found that $I = 60$ (number of MMA iterations) were sufficient. Considering the penalisation scheme, superior thermal material distributions were achieved when p is initially set to 1 (no penalisation) and incrementally increased as the MMA iterations progress. It was found that constant penalisation was detrimental to the final thermal performance. An incrementally increasing p value starting at 1 and ending at 3 at the last MMA iteration was adopted. When using an initial uniform density

distribution (with $\theta_i = V^*$) also resulted in superior distribution solutions compared with imposed material distributions, which could affect the outcome of the topology optimization scheme and which should be guarded against.

As mentioned earlier, s and s_0 which were used to control the behaviour of the MMA asymptotes, could have an effect on the converged material distribution and could therefore also influence the converged τ value. A wide range of s and s_0 value combination were tested in order to arrive at the lowest optimized value of $g_0(\mathbf{T})$. Refer to Figure 2 showing the impact of s and s_0 for an arbitrary chosen k^* and V^* scenario. It was found that $s = 0.85$ provided the lowest values of τ across a wide range of s_0 . When s_0 was set between 0.15 and 0.25, good thermal performing solutions were obtained for all other k^* and V^* scenarios considered. Based on this, $s = 0.85$ and $s_0 = 0.15$ were adopted for the entire study, but were routinely checked. For domains which are not cubic in nature, other values of s and s_0 might be suitable.

4. Partial Dirichlet Boundary

The first boundary condition that was evaluated is that of a partial Dirichlet boundary. Only the square region on one of the domain edge surfaces has a fixed uniform temperature as shown in Figure 1. All other surfaces were adiabatic, thus, heat was only able to escape the domain at the temperature boundary. This boundary type was investigated as a starting point to perform a tentative comparison with other two-dimensional studies that also utilized such a boundary type. Figure 3 shows the converged three-dimensional material distribution for an arbitrary test case with $k^* = 500$, $V^* = 0.1$, and $c/L_D = 0.1$. Black regions in the side and top views represent design variables $\theta = 1$ (placement of high thermal conductive material) while white regions represent $\theta = 0$. Grey shades represent intermediate density values ($0 < \theta < 1$). The grey shades in the isometric view have no significance other than to improve visibility of the converged three-dimensional structure.

The figure shows a tree-like structure, with four main branches extending to the outer-upper corners of the domain. The structure has a single origin, at the position of the constant temperature region. As expected, the converged material distribution is symmetric in nature. The principle-view and top-view show a surprisingly ordered structure with a large number of the secondary branches extending outwards orthogonally to the domain edges, frequently at vertical and horizontal alignments, or diagonally towards the vertical corner lines of the domain. Similar overall tree structures were observed for all partial Dirichlet boundary cases. Minor overall structural variations were present at different k^* and V^* combinations.

4.1. Results for Different Conductivity and Volume Ratios

The conductivity ratio, k^* , and maximum volume ratio, V^* , had a significant impact on the frequency and length of the branches, as well as on the thermal performance of the converged material distributions. These impacts were investigated for conductivity ratios ranging from $k^* = 5$ to 3 000 and volume ratio constraints between $V^* = 0.05$ and 0.3.

Since the three-dimensional architecture is difficult to replicate on paper, a diagonal section on plane D (as defined in Figure 1) is used to compare different scenarios with each other. Converged architectures for different values of k^* at $V^* = 0.1$ are given in Table 1, as well as the steady-state non-dimensional temperature, for each, normalised between the lowest and highest temperatures. Here black refers to the highest temperature while white refers to lowest temperature. It can be seen that the peak temperature location is different depending on the material distribution, however, normally this temperature is located somewhere on the adiabatic boundary. It might appear that some sections are disconnected from the main structure, but this is only due to the figures containing sectional views of the tree structures. The disconnected portions just indicate where a branch intercepts the sectional plane. The architectures are similar in nature to architectures obtained in two-dimensional studies [14-16], especially for k^* values greater than 500. The width of the base and the main branches decreases with an increase in the conductivity ratio. For lower k^* values, there are less secondary branches, most of which extend normally to the side of the domain. With an increase in k^* , the number of secondary branches increases and most of these extend with an upward gradient. This follows logically from the fact that a higher conductive solid requires a smaller cross-sectional area to conduct a particular heat rate through it. Due to the thinner branches, volume capacity is available for the branches to reach further into the heat-producing domain, or to branch into more secondary branches.

Table 2 contains converged architectures obtained for different values of V^* at $k^* = 500$. With the increase in V^* , the width of the main and secondary branches quickly starts to increase. Also included in this table are the converged temperature distributions for each case.

A plot of τ values for the converged material distributions with a partial Dirichlet boundary is supplied in Figure 4 with dashed lines. It shows that τ is decreased as either, or both, the conductivity ratio or the volume ratio is increased. For $k^* > 500$, relatively little enhancement in the converged thermal performance is obtained,

mainly since the length and positioning of the high conductive branches do not alter significantly as the thermal conductivity is increased further.

5. Full Dirichlet Boundary

The use of a partial Dirichlet boundary is not always representative of the thermal boundary conditions present on actual heat-producing media. Frequently, an entire surface of a rectangular heat producing solid is able to exchange heat with, for instance, a heat sink or a cold plate. To represent such cases more realistically, a full Dirichlet boundary condition (where one entire edge of the domain is at a uniform temperature of T_∞) was also considered. The problem with such a boundary condition is that if a uniform initial density distribution is used, $\partial g_0/\partial\theta$ will be constant on all x - y -planes during the initial MMA iterations. This means that the optimisation algorithm will not be able to develop observable internal conducting structures.

To counteract this, a section of the domain's material distribution was pre-defined in order to provide a seeding location as shown in Figure 5. The MMA algorithm was not allowed to alter this region. The subdomain of height of H_b , had a set of fixed θ values, with $\theta = 1$ at the locations from where main branches are to form, while all other elements in the subdomain were allocated $\theta = 0$. This provided the variation needed in $dg_0/d\theta$. In this paper one-, two- and four-seed locations are considered.

5.1. One-Seed Case

5.1.1. Subdomain Definition

A single-square seed location placed in the centre of the bottom surface of the domain was considered first. In order to determine the influence of the c and H_b on the optimized material distribution, c/L_D was ranged between 0.08 and 0.8, and H_b/L_D , was ranged between 0.04 and 1.0. It was found that an increase in the relative height of subdomain H_b/L_D , limited the domain which the MMA can modify, which resulted in increased internal temperatures. With a thinner subdomain, the optimisation procedure was better-abled to arrive at thermally more efficient material distributions.

Table 3 shows a selection of architectures for $H_b/L_D = 0.04$ for different values of c/L_D . As c/L_D increases, the main tree structure becomes "hollow", the number of secondary branches reduces and the gradient of the main branches increases, eventually to the point where the main branches are straight up, or even incline inwards.

Converged τ values for different combinations of H_b/L_D and c/L_D are given in Figure 6 for $k^* = 500$ and $V^* = 0.05$. It can be seen that the optimal value for c/L_D is approximately 0.24 for $H_b/L_D \leq 0.4$. As H_b/L_D is increased, τ increases exponentially. Similar tendencies were observed for all k^* and V^* values. Best performance was achieved when the fixed subdomain was as thin as possible. Based on this, $c/L_D = 0.24$ and $H_b/L_D = 0.04$ were used to investigate a single-seed location. Both, centred and non-centred seed locations were considered.

5.1.2. Centred seed placement results

Figure 7 represents the converged material distribution obtained with a full Dirichlet boundary type for the same k^* and V^* case shown in Figure 3, which was obtained with the partial Dirichlet boundary type. The similarities can be clearly seen, with the main branches again extending to the corners of the domain. The main branches are, however, thinner for the full Dirichlet boundary compared with the partial boundary, especially when considering the top view. Even though $c/L_D = 0.25$ instead of $c/L_D = 0.1$, the main trunk in the middle is also smaller for the full Dirichlet boundary. In terms of the secondary branches, there are fewer branches for the full Dirichlet boundary compared with the partial boundary.

Figure 4 also plots the τ values obtained for the converged material distributions for a full Dirichlet boundary (solid lines) over a range of k^* and V^* values. For comparative purposes, the τ values as obtained with a partial and full Dirichlet boundary are plotted on the same graph. The full Dirichlet boundary exhibits a significant reduction in temperatures due to the larger boundary surface area at a low constant temperature. As before, increases in either k^* or V^* lead to reduced internal temperatures.

Some sectional views of converged architectures are given in Table 4 for $V^* = 0.1$ at for different values of k^* . As seen, the architectures obtained with the full Dirichlet boundary are similar to those obtained earlier for the partial Dirichlet boundary, except at low k^* values where additional tree structures form at location other than the intended seeding point. Due to the predefined subdomain, these additional structures are not linked to the outer surface of the domain. In general, there are fewer secondary branches present for the full Dirichlet boundary than for the partial boundary.

5.1.3. Non-centred seed placement results

Non-centred placement of a single-seed location at x and y directional offset values of x_1 and y_1 respectively is now considered. The same c/L_D and H_b/L_D values were used as before. The thermal performances of the resulting converged material distributions are given in Figure 8 for $V^* = 0.05$ and $k^* = 500$. As shown, a centred seed location at $x_1 = y_1 = 0$ results in the best optimized material distribution. The same finding was obtained for all V^* and k^* cases.

Even for off-centre seed placements, four main branch structures were obtained, each extending in a straight path towards the furthest domain corners as demonstrated in Table 5 for architectures viewed from below. The branch that extends to the furthest corner is the best developed. Several sub-branches are also present.

5.2. Two-Seed Case

Two main configuration types for the placement of two-seed locations, as shown in Figure 9, were considered. Each seed location had dimension c by c in the x - y -plane. As before, different c/L_D and H_b/L_D values for the subdomain definition were investigated for a wide range of x_2 , y_2 , k^* , and V^* . It was found that $c/L_D = 0.24$ and $H_b/L_D = 0.04$ for each seed location respectively produced the best-performing optimized material layouts.

Figure 10 shows the influence of the placement of the seed locations for the c/L_D and H_b/L_D values when considering configuration I for $V^* = 0.05$ and $k^* = 500$. Similar trends were observed for all other V^* and k^* values. From the figure, it can be seen that the optimisation algorithm produced the best-performing material distributions when $x_2/L_D = 0.25$ and $y_2/L_D = 0$. The same seed placement ($y_2/L_D = 0$ and $x_2/L_D = 0.25$) was attained when Configuration II was considered (not shown here).

A representative material distribution is given in Figure 11 for $V^* = 0.05$ and $k^* = 500$ for this seed placement. It can be seen that two identical, mirror-imaged, non-merging structures are present. From the top view, it can be seen that each has four main branches. From the front and side views, it can be seen that these branches extend towards the corners of each half-domain, similar to the case with a single-tree structure that extended towards the four upper corners of the full domain. Several secondary branches developed also.

The influence of V^* and k^* on the converged τ is given in Figure 12. At first glance, there is little or no improvement in the thermal performance when using two seeding locations compared with one seeding location (compared with the single-seed location plot in Figure 4). However, finer comparisons reveal that the τ values

are indeed decreased. By making use of Eq. (17), the performance improvement (expressed in terms of a reduction in temperature) can be calculated.

$$Performance\ difference(\%) = \frac{|\tau_1 - \tau_2|}{\tau_1} * 100 \quad (17)$$

Here subscript 1 refers to the single-seed case and subscript 2 to the two-seed case. As example: τ decreased by 4% for a $k^* = 50$ and $V^* = 0.05$, and by 11% for $k^* = 1000$, $V^* = 0.05$ when using two seed locations compared with one location.

5.3. Four-Seed Case

Four-seed locations, as described in Figure 13, are considered now with each seed location again having dimensions c by c in the x - y -plane. For this configuration, $c/L_D = 0.12$ and $H_b/L_D = 0.04$ resulted in the best-performing material distributions. The positioning of the seed locations was investigated, as was done with the single-seed and two-seed cases. As expected, the best performance was achieved when $x_4/L_D = y_4/L_D = 0.25$. This describes the case where the seed locations are equally distributed on the lower surface of the domain.

Figure 14 shows a material distribution for $V^* = 0.05$ and $k^* = 500$, using four seed locations. In this case, four identical, non-merging structures are present. From the top view, it can be seen that each tree structure again has four main branches. From the front and side views, it can be seen that these branches extend towards the corners of each quarter-domain, similar to the single-seed and two-seed cases. Secondary branches are present, but are considerably smaller when compared with secondary branches from the one-seed and two-seed cases. Also, there are much fewer secondary branches present.

The influence of V^* and k^* follows the same trend as with the one-seed and two-seed cases and is not shown here. Using four locations improved the thermal performance compared with the two-seed case (which already showed improved compared with the one-seed case).

5.4. Comparison of Thermal Performance

Figure 15 shows the performance improvement (in terms of a reduction in the non-dimensional temperature) when using multiple seed locations compared with the one-seed case. An arbitrarily chosen scenario with $V^* =$

0.05 is considered for a wide range of k^* values, where 1-2 denotes the decrease in τ when using two seed locations compared with one as is defined by Eq. (17). The same applies to 1-4.

From Figure 15 it is evident that the two-seed case resulted in tree structures that perform better than those with the single-seed case. A larger improvement is obtained when four seed locations were used. For low conductivity values ($k^* \leq 20$), the performance increase gained with multiple seed locations was relatively low, compared to the improvements obtained in the mid-conductivity range. Of all the cases considered for $V^* = 0.05$, a maximum decrease of 20% in the maximum temperature was observed for $k^* = 500$, when increasing the initial seed points from one to four.

6. Conclusion

The optimum layout of heat-conducting paths in a three-dimensional heat-producing cubic domain as obtained with topology optimisation, using the method of moving asymptotes (MMA) algorithm, was investigated. Converged high conductive material distributions resembling natural tree-structures were obtained. When using a partial Dirichlet boundary and a centred single-seed location, the architectures were similar in nature to those obtained in two-dimensional studies, except that four main branches were obtained, each of which extended towards an upper domain corner. When non-centred seed positions were considered, non-symmetric tree structures, still with four main branches present, were obtained. The thermal performance of such material distributions was inferior to those that used a centred seed location.

A full Dirichlet boundary was also investigated for two-seed, and four-seed location cases. This required a fixed defined subdomain (which could not be altered by the optimisation algorithm). This subdomain was optimized to enable the MMA algorithm to develop the best-performing tree structures. This included the determination of the optimal relative placement (x_1/L_D and y_1/L_D) of the seed locations, the relative height (H_b/L_D) and the relative size of each (c/L_D). For each seed location, a separate tree structure was obtained. Each tree structure had four main branches extending towards the corners of the imaginary rectangular subdomain surrounding it.

For optimally placed multiple seed locations for a full Dirichlet boundary, thermal performance increased as the number of seed locations increased from one to two and from two to four, for all volume ratios and conductivity ratios. Overall, by using four seed positions, the thermal performance was improved by up to 23% compared to when a single seed position was used for a volume ratio of 0.05 and a conductivity ratio of 500.

7. References

- [1] A. Bejan, Constructal-theory network of conducting paths for cooling a heat generating volume, *Int. J. Heat Mass Transfer* 40 (4) (1997), 799–816.
- [2] M. Neagu, A. Bejan, Constructal placement of high-conductivity inserts in a slab: optimal design of roughness, *J. Heat Transfer* 123 (6) (2001), 1184–1189.
- [3] M. Almgöbel, A. Bejan, Constructal optimization of nonuniformly distributed tree-shaped flow structures for conduction, *Int. J. Heat Mass Transfer* 44 (22) (2001), 4185–4194.
- [4] A. Bejan, M. Almgöbel, Constructal T-shaped fins, *Int. J. Heat Mass Transfer* 43 (12) (2000), 2101–2115.
- [5] A. Alebrahim, A. Bejan, Constructal trees of circular fins for conductive and convective heat transfer, *Int. J. Heat Mass Transfer* 42 (19) (1999), 3585–3597.
- [6] L.A.O. Rocha, S. Lorente, A. Bejan, Conduction tree networks with loops for cooling a heat generating volume, *Int. J. Heat Mass Transfer* 49 (15-16) (2006), 2626–2635.
- [7] A. K. da Silva, C. Vasile, A. Bejan, Disc cooled with high-conductivity inserts that extend inward from the perimeter, *Int. J. Heat Mass Transfer* 47 (19-20) (2004), 4257–4263.
- [8] L. Gosselin, A. Bejan, Constructal heat trees at micro and nanoscales, *J. Applied Physics* 96 (10) (2004), 5852–5859.
- [9] J. Dirker, A. G. Malan, J. P. Meyer, Thermal characterisation of rectangular cooling shapes in solids, *Int. Journal Numerical Methods Heat Fluid Flow* 17 (4) (2007), 361–383.
- [10] J. Dirker, J. P. Meyer, Thermal characterisation of embedded heat spreading layers in rectangular heat-generating electronic modules, *Int. J. Heat Mass Transfer* 52 (5-6) (2009), 1374–1384.
- [11] J. Dirker, J. P. Meyer, Heat removal from power electronics in two-direction sets using embedded solid state cooling layers – A proposed non-numerical calculation method, *J. Heat Transfer Engineering* 30 (6) (2009), 452–465.
- [12] R. Boichot, L. Luo, Y. Fan, Tree-network structure generation for heat conduction by cellular automaton, *Energy Conversion and Management* 50 (2) (2009), 376–386.

- [13] B. Song, Z. Guo, Robustness in the volume-to-point heat conduction optimization problem, *Int. J. Heat Mass Transfer* 54 (21-22) (2011), 4531–4539.
- [14] A. Gersborg-Hansen, M. P. Bendsøe, O. Sigmund, Topology optimization of heat conduction problems using the finite volume method, *Structural and Multidisciplinary Optimization* 31 (4) (2006), 251–259.
- [15] Y. Zhang, S. Liu, Design of conducting paths based on topology optimization, *Heat and Mass Transfer* 44 (10) (2008), 1217–1227.
- [16] J. Dirker, J. P. Meyer, Topology optimization for an internal heat-conduction cooling scheme in a square domain for high heat flux applications, Accepted for publication: *J. of Heat Transfer* (In Press Manuscript ID: HT-12-1239, DOI: 10.1115/1.4024615).
- [17] Q. Li, G.P. Steven, Y.M. Xie, O.M. Querin, Evolutionary topology optimization for temperature reduction of heat conducting fields, *Int. J. Heat Mass Transfer* 47 (23) (2004), 5071–5083.
- [18] Q. Li, G. P. Steven, O. M. Querin, Y. M. Xie, Shape and topology design for heat conduction by Evolutionary Structural Optimization, *Int. J. Heat Mass Transfer* 42 (17) (1999), 3361–3371.
- [19] T. Gao, W. H. Zhang, J. H. Zhu, Y. J. Xu, D. H. Bassir, Topology optimization of heat conduction problem involving design-dependent heat load effect, *Finite Elements in Analysis and Design* 44 (14) (2008), 805–813.
- [20] X. Cheng, Z. Li, Z. Guo, Constructs of highly effective heat transport paths by bionic optimization, *Science in China Series E: Technological Sciences* 46 (3) (2003), 296–302.
- [21] X. Xu, X. Liang, J. Ren, Optimization of heat conduction using combinatorial optimization algorithms, *Int. J. Heat Mass Transfer*, 50 (9-10) (2007), pp. 1675–1682
- [22] G.A. Ledezma, A. Bejan, Constructal three-dimensional trees for conduction between a volume and a point, *J. Heat Transfer* 120 (4) (1998), 977–984.
- [23] M. Neagu, A. Bejan, Three-dimensional tree constructs of ‘constant’ thermal resistance, *J. Applied Physics* 86 (12) (1999), 7107–7115.

- [24] H.Feng, L. Chen, F. Sun, "Volume-point" heat conduction constructal optimization based on entransy dissipation rate minimization with three-dimensional cylindrical element and rectangular and triangular elements on microscale and nanoscale, *Science China Technological Sciences* 55 (3) (2012), 779–794.
- [25] K.-T. Zuo, L.-P. Chen, Y.-Q. Zhang, J. Yang, Study of key algorithms in topology optimization, *Int. J. Advanced Manufacturing Technology* 32 (7-8) (2007), 787–796.
- [26] M. Bruyneel, P. Duysinx, and C. Fleury, A family of MMA approximations for structural optimization, *Structural and Multidisciplinary Optimization* 24 (4) (2002), 263–267.
- [27] L. F. P. Etman, A. A. Groenwold, J. E. Rooda, First-order sequential convex programming using approximate diagonal QP subproblems, *Structural and Multidisciplinary Optimization* 45 (4) (2012), 479–488.
- [28] K. Svanberg, The method of moving asymptotes - a new method for structural optimization, *Int. J. for Numerical Methods in Engineering* 24 (2) (1987), 359–373.
- [29] G. Strang, *Computational Science and Engineering*, Wellesley-Cambridge Press, Wellesley, 2007, p. 678
- [30] S.Zhou, L. Chen, F. Sun, Optimization of constructal volume-point conduction with variable cross section conducting path, *Energy Conversion and Management* 48 (1) (2007), 106–111.

List of Figures

Figure 1: Schematic diagram for a partial Dirichlet boundary using a three-dimensional domain.

Figure 2: The effect of the initial asymptote setting, s_0 and s , on τ for an arbitrary chosen scenario.

Figure 3: Sample solution obtained for $k^* = 500$, $V^* = 0.1$, $c/L_D = 0.1$ for a partial Dirichlet boundary.

Figure 4: Comparison of the converged thermal performance for different volume ratio constraints and conductivity ratios for full and partial Dirichlet boundary types.

Figure 5: Domain for the full Dirichlet boundary with a single-seed location.

Figure 6: The effect of the seed size and height for $k^* = 500$ for a full Dirichlet boundary.

Figure 7: Sample solution obtained for $k^* = 500$, $V^* = 0.05$, $c/L_D = 0.24$, and $H_b/L_D = 0.04$ for a full Dirichlet boundary.

Figure 8: The effect on τ due to the position of a single-seeding location for a full Dirichlet boundary for $V^* = 0.05$ and $k^* = 500$.

Figure 9: Configurations I and II for the placement with the two-seed case.

Figure 10: The influence of the placement of two-seed locations according to Configuration I for $V^* = 0.05$ and $k^* = 500$.

Figure 11: A converged architecture for the two-seed case with $k^* = 500$ and $V^* = 0.05$.

Figure 12: Influence of V^* and k^* on τ for the two-seed case with $x_2/L_D = 0.25$ and $y_2/L_D = 0$.

Figure 13: Four-seed case configuration.

Figure 14: A converged architecture for the four-seed case with $k^* = 500$ and $V^* = 0.05$.

Figure 15: The performance increase when using multiple seed locations for $V^* = 0.05$ and varying values of k^* using a three-dimensional domain with full Dirichlet boundary.

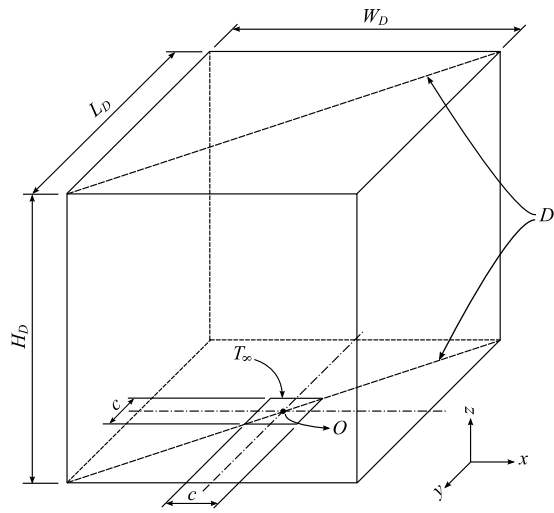


Figure 1

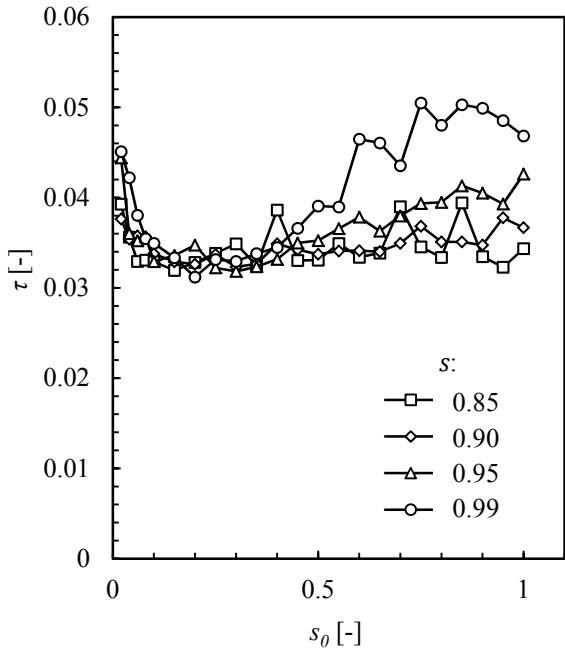


Figure 2

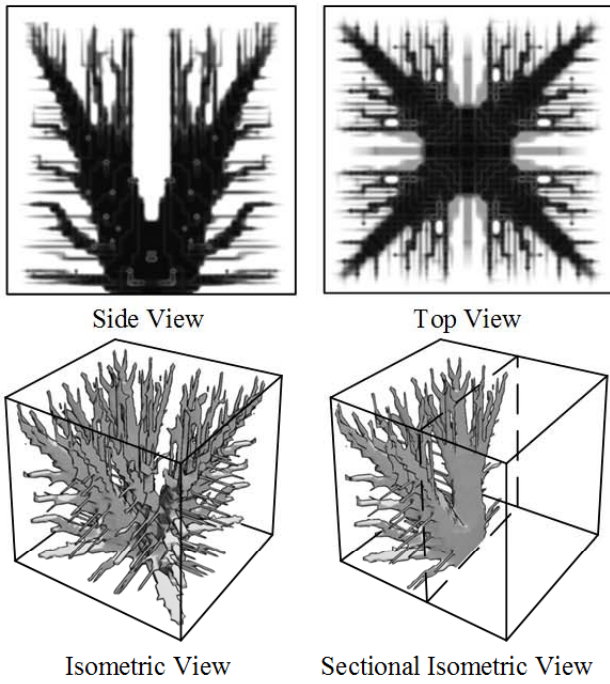


Figure 3

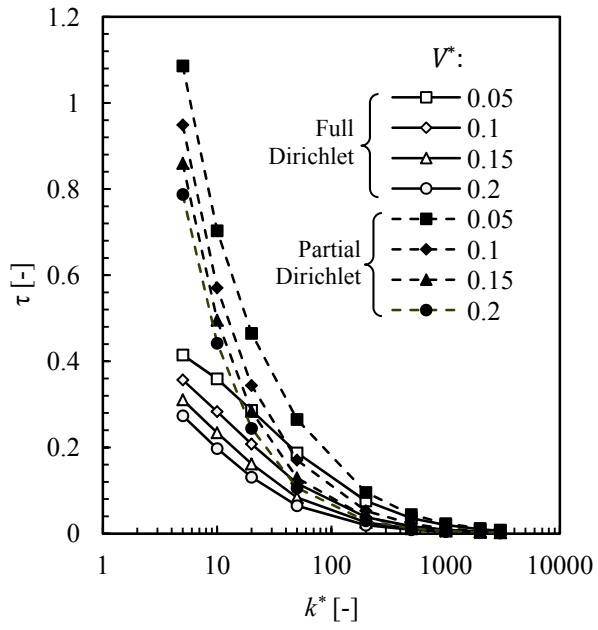


Figure 4

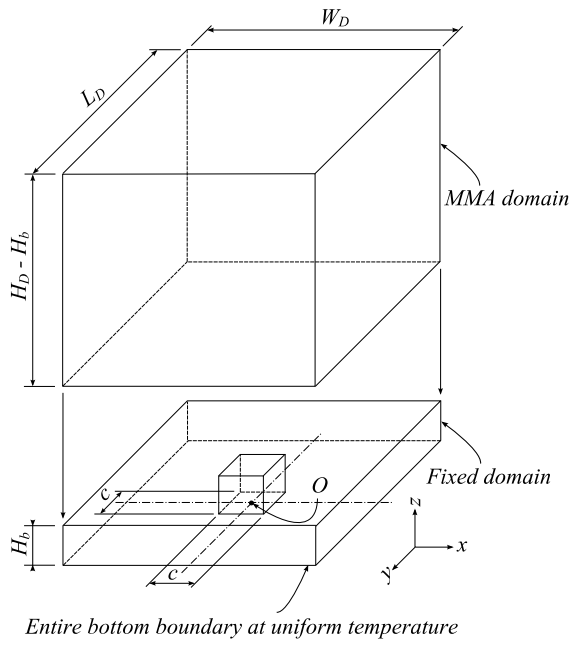


Figure 5

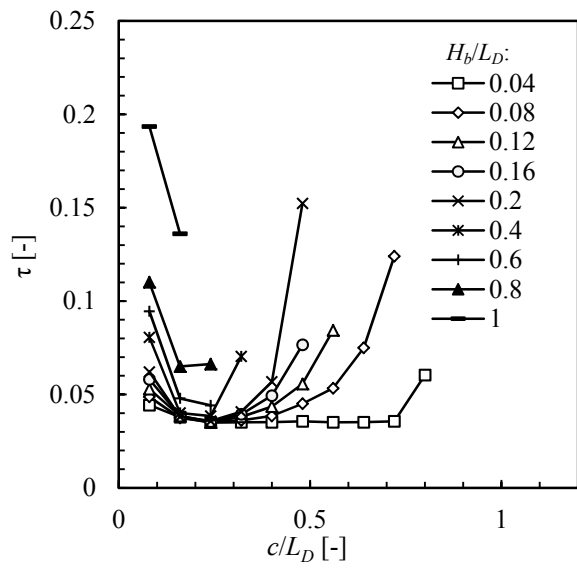
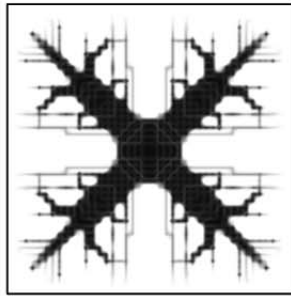


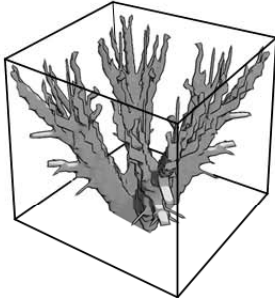
Figure 6



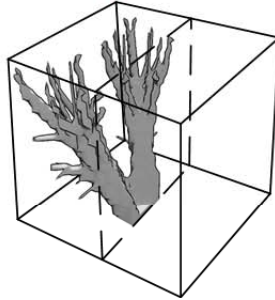
Side View



Top View



Isometric View



Sectional Isometric View

Figure 7

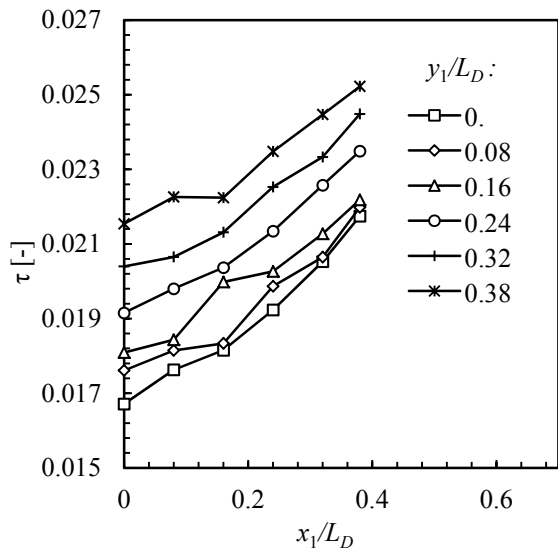


Figure 8

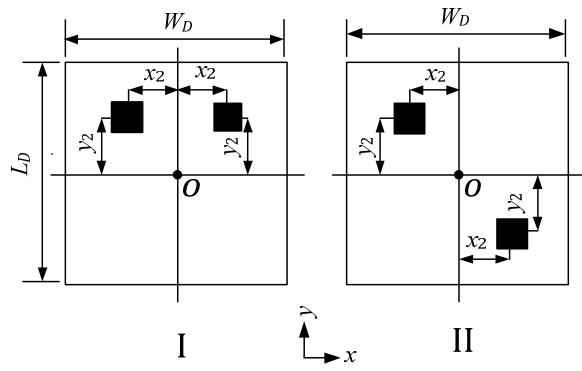


Figure 9

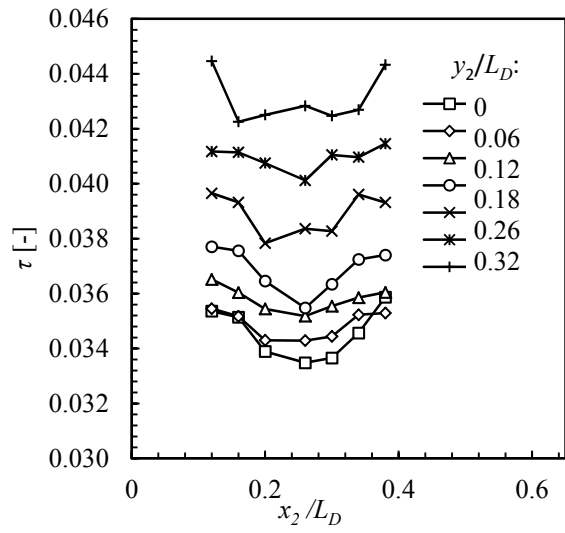
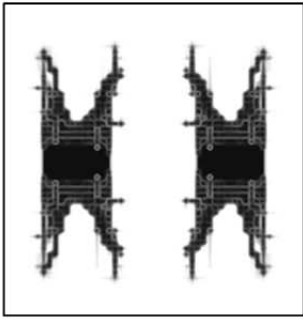
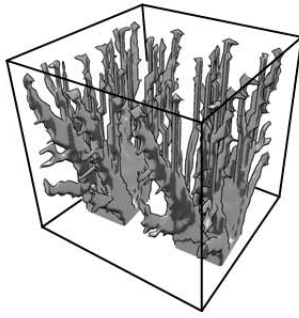


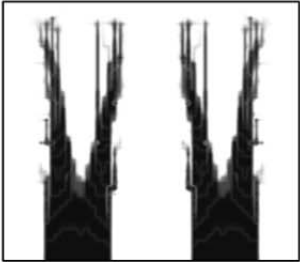
Figure 10



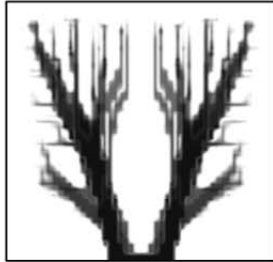
Top View



Isometric View



Front View



Side View

Figure 11

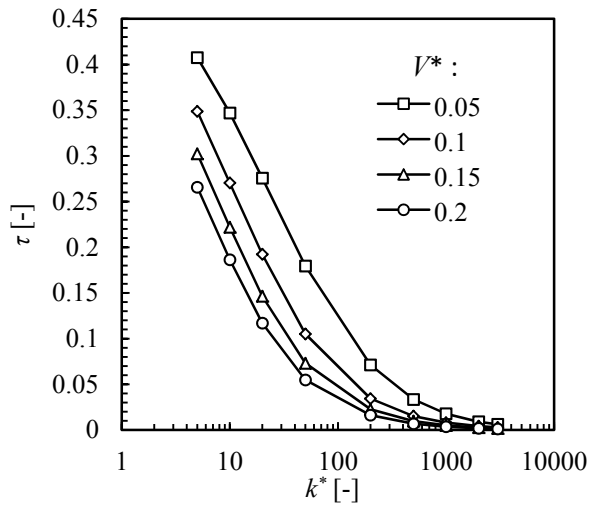


Figure 12

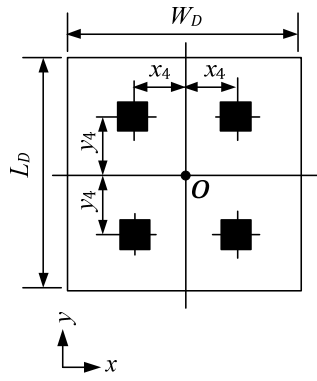


Figure 13

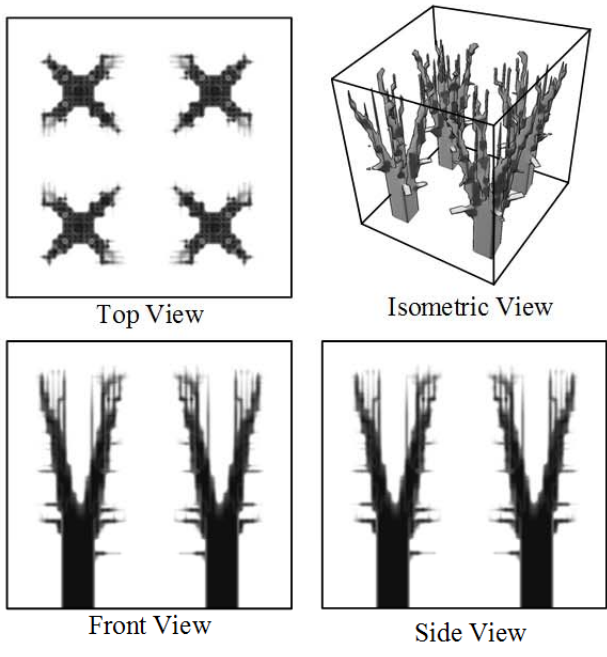


Figure 14

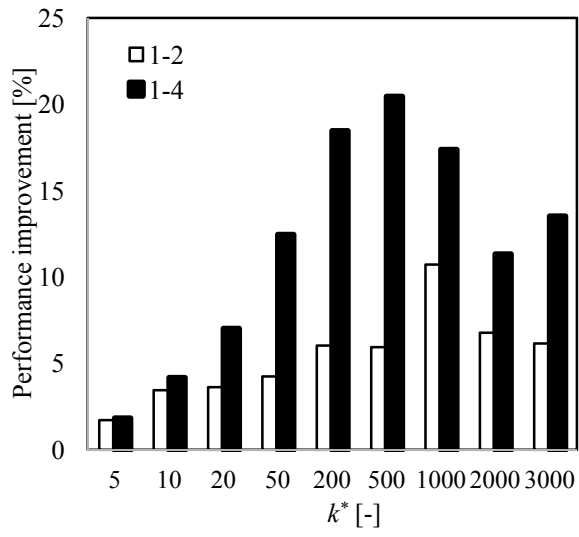


Figure 15

List of Tables

Table 1: Impact of the conductivity ratios for $V^* = 0.1$ and $c/L_D = 0.1$ with a partial Dirichlet boundary.

Table 2: Impact of the volume ratio constraint for $k^* = 500$ and $c/L_D = 0.1$ with a partial Dirichlet boundary.

Table 3: Comparison of architectures for different values of c/L_D using $k^* = 500$, $H_b/L_D = 0.04$ and $V^* = 0.05$ for a full Dirichlet boundary.

Table 4: Architectures for the different conductivity ratios at $V^* = 0.1$, $c/L_D = 0.24$, and $H_b/L_D = 0.04$ for a full Dirichlet boundary on section D.

Table 5: Architectures viewed from below for non-centred seed locations for $k^* = 500$ and $V^* = 0.05$.

Table 1













$k^* [-]$	5	50	500
$\tau [-]$	9.487×10^{-1}	1.704×10^{-1}	2.268×10^{-2}
θ			
T			
$k^* [-]$	1000	2000	3000
$\tau [-]$	1.145×10^{-2}	6.312×10^{-2}	4.090×10^{-3}
θ			
T			

Table 2













$V^* [-]$	0.05	0.1	0.15
$\tau [-]$	4.420×10^{-2}	2.268×10^{-2}	1.538×10^{-2}
θ			
T			
$V^* [-]$	0.2	0.25	0.3
$\tau [-]$	1.192×10^{-2}	1.091×10^{-2}	8.458×10^{-2}
θ			
T			

Table 3

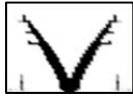





$c/L [-]$	0.08	0.24	0.40
$\tau [-]$	4.431×10^{-2}	3.495×10^{-2}	3.516×10^{-2}
θ			
$c/L [-]$	0.56	0.72	0.80
$\tau [-]$	3.514×10^{-2}	3.564×10^{-2}	6.041×10^{-2}
θ			

Table 4







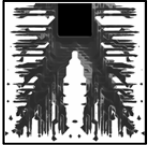

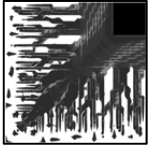
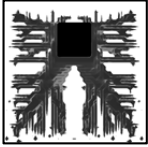

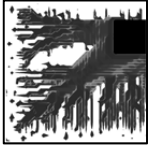
$k^* [-]$	5	50	500
$\tau [-]$	3.567×10^{-1}	1.164×10^{-1}	1.693×10^{-2}
θ			
$k^* [-]$	1000	2000	3000
$\tau [-]$	8.839×10^{-3}	4.618×10^{-3}	3.293×10^{-3}
θ			

Table 5

y_1/L_D	x_1/L_D		
	0	0.24	0.38
0.38			
0.24			
0	